Selective anodes for seawater splitting via functionalization of manganese oxides by a plasma-assisted process

Lorenzo Bigiani[a], Davide Barreca[b,*], Alberto Gasparotto[a], Teresa Andreu[c,d], Johan Verbeeck[e], Cinzia Sada[f], Evgeny Modin[g], Oleg I. Lebedev[h], Juan Ramón Morante[c,d], and Chiara Maccato[a,**]

[a]Department of Chemical Sciences, Padova University and INSTM, 35131 Padova, Italy

[b]CNR-ICMATE and INSTM, Department of Chemical Sciences, Padova University, 35131 Padova, Italy

[c]Catalonia Institute for Energy Research (IREC), Sant Adrià de Besòs, 08930 Barcelona, Spain

[d]Universitat de Barcelona (UB), 08028 Barcelona, Spain

[e]EMAT and NANOlab Center of Excellence, University of Antwerp, 2020 Antwerpen, Belgium

[f]Department of Physics and Astronomy, Padova University and INSTM, 35131 Padova, Italy

[g]CIC nanoGUNE BRTA, 20018 Donostia - San Sebastian, Spain

[h]Laboratoire CRISMAT, UMR 6508 CNRS/ENSICAEN/UCBN, 14050 Caen Cedex 4, France

* Corresponding author. Tel: +39-049-8275170; E-mail: davide.barreca@unipd.it (Davide Barreca)

** Corresponding author. Tel: +39-049-8275234; E-mail: chiara.maccato@unipd.it (Chiara Maccato)

Graphical Abstract
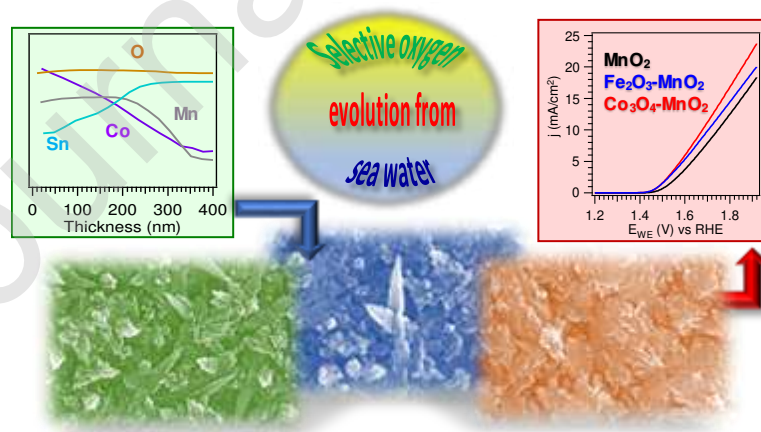
Highlights

- MnO_2 and Mn_2O_3 decorated with Fe_2O_3 or Co_3O_4 are fabricated by a plasma-assisted

approach.

- The developed systems are tested as anodic catalysts for oxygen evolution from seawater.

- MnO_2-Co_3O_4 yields an outstanding Tafel slope of ≈ 40 mV$\times$dec^{-1} and an overpotential of 450 mV, excluding chlorine evolution.

- The catalyst performances and durability could contribute to sustainable H_2 production from seawater for practical end-uses.

Abstract

The electrolysis of seawater, a significantly more abundant natural reservoir than freshwater, stands as a promising alternative for sustainable hydrogen production, provided that the competitive chloride electrooxidation is minimized. Herein, we propose an original material combination to selectively trigger oxygen evolution from seawater at expenses of chlorine generation. The target systems, based on MnO_2 or Mn_2O_3 decorated with Fe_2O_3 or Co_3O_4, are fabricated by plasma enhanced-chemical vapor deposition of manganese oxides, functionalization with Fe_2O_3 and Co_3O_4 by sputtering, and annealing in air/Ar to obtain Mn(IV)/Mn(III) oxides. Among the various options, MnO_2 decorated with Co_3O_4 yields the best performances in alkaline seawater splitting, with an outstanding Tafel slope of ≈ 40 mV$\times$dec^{-1} and an overpotential of 450 mV, enabling to rule out chlorine evolution. These attractive performances, resulting from the synergistic contribution of catalytic and electronic effects, open the door to low-cost hydrogen generation from seawater under real-world conditions, paving the way to eventual large-scale applications.

Keywords: Manganese oxides; Plasma enhanced-chemical vapor deposition; Sputtering; Oxygen evolution reaction; Seawater splitting

1. Introduction

The concept of green hydrogen economy has been increasingly considered as an alternative

2

scenario to suppress the release of CO_2 and other contaminants produced by the extensive use of fossil fuels [1-11]. Besides being an excellent energy carrier, hydrogen can be used either in fuel cells, or, in turn, to generate other synthetic fuels [12-16]. Among the various routes to H_2, water electrolysis is an outstanding option [10-11,17-21], and its use has been investigated with many electrocatalysts operated in freshwater comprising acids, bases or buffer systems [18,22-25]. Nevertheless, the high cost of oxygen evolution catalysts, traditionally based on rare/expensive metals (*e.g.* RuO_2, IrO_2,…) and suffering from an insufficient long-term stability [1,5,18,26], hinders the large scale diffusion of commercial electrolyzers and has stimulated research on alternative oxide materials [6,21,24,27]. On the other hand, an additional bottleneck hampering the widespread use of water electrolysis is the limited availability of pure H_2O feedstocks, especially in hot/arid zones [4,12,14]. A feasible route to circumvent this difficulty is the use of seawater [1,12,28-30], the most Earth-abundant water reservoir (> 95% of the total H_2O), possessing also a fairly homogeneous geographical distribution [9,31-32]. In fact, seawater electrolysis could be conveniently driven by renewable electricity (either wind-based, or from photovoltaics) in solar energy-rich coastal/arid regions, yielding a sustainable H_2 production of key importance for the future energy landscape [12-14,19,29,33]. However, the utilization of seawater in electrolytic devices remains a challenging task especially for the strongly demanding conditions of the anode [9,28]. In fact, the presence of an overall salt concentration of ≈ 3.5 wt.% [12,31-32] renders the oxidation of chloride species to Cl_2 (chlorine evolution reaction, CER; $2Cl^- \rightarrow Cl_2 + 2e^-$) more kinetically favorable [12,29], and hence competitive with water oxidation to O_2 (oxygen evolution reaction, OER; $4OH^- \rightarrow O_2 + 2H_2O + 4e^-$) [9,29,34]. As a matter of fact, Cl_2 is a major building block for both the chemical and pharmaceutical industry not only as a disinfectant, but also to manufacture polyvinyl chloride-based plastics and inorganic compounds, as well as to experiment and implement newly synthesized molecules, thanks to its low cost and ease of processing. Nonetheless, it is

worthwhile noting that chlorine storage and transport are hampered by its corrosivity and toxicity [34], and that the chlorine amount that would be produced to supply the world with hydrogen would rapidly exceed the demand [28]. As a matter of fact, OER is a sluggish four-electron transfer reaction, limiting the overall water splitting efficiency due to the high overpotential (η) [5-6,35-38]. In this regard, an open challenge lies in the manufacturing of stable anodes selectively triggering OER against CER, to boost seawater electrolysis towards the best performances attainable with freshwater, and empower its extensive exploitation for hydrogen production. Furthermore, hypochlorite (ClO$^-$) formation, with an onset at η values close to 480 mV, could compete with OER during the target process. This issue highlights the need of highly active OER electrocatalysts yielding high currents in H$_2$O electrolysis at overpotentials well below hypochlorite formation [28].

In general, previous literature studies on seawater electrolysis can be classified into three main types, depending on the operation: 1) under neutral conditions, with a permselective layer on a catalyst (such as IrO$_2$) [1,34]; 2) under neutral conditions, using OER selective catalysts [39-40]; 3) under alkaline conditions [14,28]. The latter enable the use of non-noble metal catalysts and yield high OER selectivity [4,14,28,31-32], since the OER potential decreases with increasing pH [28], whereas CER, with a pH-independent potential, prevails in acidic media [9,32]. In addition, if the process is carried out in alkaline media at η values < 480 mV, no appreciable ClO$^-$ formation from chloride oxidation occurs, and OER takes place exclusively [9,14,16,31-32].

In spite of different works on anodic catalysts for seawater electrolysis [9,14,17,28], materials selective towards OER are, in general, rather rare and suffer from a limited durability [1,9,28-29]. A noteworthy exception is offered by abundant, low-cost and environmentally friendly manganese oxides [19-20,33], among which MnO$_2$ [35,41-42] and Mn$_2$O$_3$ [33,42-43] have been investigated by various researchers. To boost the system OER activity, a valuable

4

strategy is the fabrication of metal oxide-based composites, yielding an improved charge carrier separation through the formation of heterojunctions and benefiting from synergistic catalytic effects between the system components [2,20,44]. To date, various reports are available on OER anodes used in freshwater comprising Mn_2O_3, as well as its composites with Ag [20], TiO_2 [10], Cr_2O_3 [18], Co_3O_4 [22], RuO_2 [2], and mixed-phase Mn_2O_3/MnO_2 systems [16]. Other works have proposed the use of MnO_2 anodes [19], as well as its composites with Au [25-26], TiO_2 [35], and Fe_2O_3 [44]. Nevertheless, the use of manganese oxide-based anodes in seawater electrolysis has been reported only in a few cases. In this regard, the pioneering work of Bennett [45] focused on a poorly crystallized MnO_2 form, whereas Izumiya *et al*. showed the favorable OER effect exerted by Mn_2O_3 functionalization with WO_3 [46-47]. Vos *et al.* [1] reported that deposition of MnO_x onto IrO_x shifted the product selectivity towards O_2, evidencing however that MnO_x as such was catalytically inactive [1,4]. Among the possible functionalizing agents, iron and cobalt oxides (in particular, Fe_2O_3 and Co_3O_4) are well-known and attractive OER catalysts thanks to their peculiar reactivity [8,18,22,35,48-49], and their combination with Mn oxides may provide technologically useful OER activities [23]. Nonetheless, to the best of our knowledge, no reports on MnO_2 and Mn_2O_3 anodes functionalized with Fe oxides for OER under dark conditions are available, whereas Co_3O_4-Mn_2O_3 anodes have been reported only once [22]. On this basis, the properties-activity interplay of Mn oxide-based composites deserves further attention to develop stable and selective anodes for OER in seawater. For the full exploitation of electrocatalyst potential in real-world end uses, the direct growth of catalysts onto conductive substrates is a preferred choice, since loading powders with binders on current collectors might result in high transport resistance, limited stability and modest performances [2,8,48,50]. Specifically, a rational nano-organization design *via* suitable fabrication routes can enhance electron transfer efficiency and ion diffusion rate, favorably influencing the ultimate system activity [8,17,43,48].
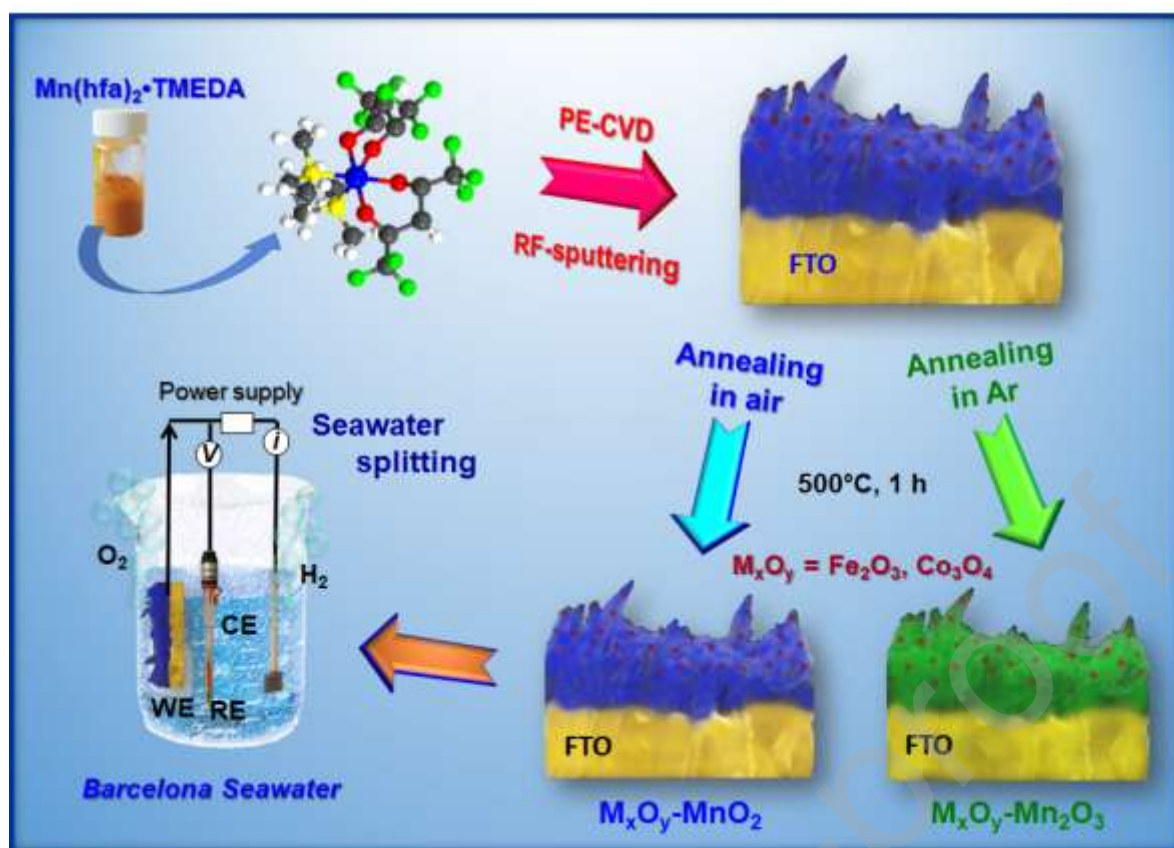
Scheme 1. Sketch of the fabrication procedure for MnO_2 and Mn_2O_3 electrodes, functionalized with Fe_2O_3 or Co_3O_4, for seawater splitting. WE = working electrode; RE = reference electrode; CE = counter-electrode.

In the present work, we report on the fabrication of stable manganese oxide-based anodes enabling oxygen evolution from seawater electrolysis with high efficiency and selectivity. Our attention is focused on MnO_2 and Mn_2O_3 nanosystems, eventually functionalized with Fe_2O_3 or Co_3O_4 nanoparticles. The present materials are developed by means of a two-step strategy, based on the plasma enhanced-chemical vapor deposition (PE-CVD) of manganese oxides on fluorine-doped tin oxide (FTO)-coated glass substrates, followed by the subsequent dispersion of Fe_2O_3 or Co_3O_4 by radio frequency (RF)-sputtering (Scheme 1). The final thermal treatment under air or inert atmospheres yields the formation of MnO_2- or Mn_2O_3-based systems, respectively. This versatile and scalable procedure enables to tailor both the composition and the morphology of the resulting systems and to obtain a chemically intimate contact between their constituents [49,51]. The latter feature, in turn, yield a reduced charge resistance, an

6

enhanced OER activity and guarantee an improved electrode stability [15,17].

To assess the applicative potential of the manufactured materials, after a detailed chemico-physical characterization, the target systems were tested as anodes for the splitting of simulated and natural seawater under alkaline conditions, similar to those of industrial electrolyzers [9,11,14]. The obtained results show that the most favorable option is based on MnO_2 decorated with Co_3O_4, whose performances (Tafel slope of ≈ 40 mV×dec^{-1} and overpotential of 450 mV at 10 mA×cm^{-2} for the best performing sample) were competitive and/or improved with respect to most oxide systems proposed for seawater splitting so far. These issues, along with the durability up to six months of prolonged utilization, highlight the validity of the present preparation strategy to manufacture anode materials endowed with excellent selectivity towards oxygen evolution.

2. Experimental Section

2.1 Material preparation

The synthesis of the target systems was performed by the initial PE-CVD of MnO_2 onto pre-cleaned [9] FTO-coated glass slides (Aldrich®; ≈ 7 Ω×sq^{-1}; FTO layer thickness ≈ 600 nm), mounted on the grounded electrode of a custom-built plasmochemical reactor, whereas RF-power (13.56 MHz) was delivered to a second electrode. Depositions were performed using electronic grade Ar/O_2 plasmas, starting from Mn(hfa)$_2$TMEDA (hfa = 1,1,1,5,5,5-hexafluoro-2,4-pentanedionate; TMEDA = *N*,*N*,*N'*,*N'*- tetramethylethylenediamine [52] as Mn molecular precursor. Basing on previous results [53], growth processes were performed using the following operating conditions: temperature = 300°C; RF-power = 20 W; total pressure = 1.0 mbar; duration = 60 min. The precursor was vaporized at 70°C in an external glass reservoir, and its vapors were delivered into the reactor through an Ar flow (rate = 60 standard cubic centimeters per minute (sccm)). Two independent inlets were used to introduce Ar (rate = 15

7

sccm) and O_2 (rate = 5 sccm) directly into the reaction chamber. The obtained materials were functionalized with Fe_2O_3 and Co_3O_4 nanoparticles by RF-sputtering from Ar plasmas, using Fe or Co targets (Alfa Aesar, Fe: 99.995%, thickness = 0.25 mm; Co: 99.95%, thickness = 0.30 mm) mounted on the RF electrode and the above obtained manganese oxide specimens as substrates on the grounded electrode. Following a preliminary experiment optimization, depositions were performed using the following settings: temperature = 60°C; RF-power = 20 W, total pressure = 0.3 mbar; Ar flow rate = 10 sccm; duration = 180 and 120 min for iron and cobalt sputtering, respectively. The resulting materials were finally subjected to a thermal treatment for 60 min at 500°C, in air or Ar atmosphere to obtain MnO_2- or Mn_2O_3-based electrodes [24], respectively.

2.2 Chemico-physical characterization

X-ray photoelectron spectroscopy (XPS) analysis was carried out on a Perkin−Elmer Φ 5600ci system, using a non-monochromated AlKα excitation source (hν = 1486.6 eV). Charging correction on binding energy (BE) values (uncertainty = ± 0.1 eV) was carried out using the C1s peak at 284.8 eV. Atomic percentages (at.%) were obtained by peak integration using Φ V5.4A sensitivity factors. Data processing involved a Shirley-type background subtraction, and, when necessary, spectral deconvolution through the XPSPEAK 4.1 software. Cobalt Auger parameter (α) was determined as the sum of $BE(Co2p_{3/2})$ and the CoLMM Auger peak kinetic energy (KE) [54]:

$$\alpha = BE(Co2p_{3/2}) + KE(CoLMM) \tag{1}$$

Iron and cobalt molar fractions were determined as [49,51]:

$$X_A = ((A \text{ at.\%}) / (A \text{ at.\%} + Mn \text{ at.\%}) \times 100) \tag{2}$$

where A = Fe, Co. Calculation yielded X_{Fe} = 39.0% and 16.0% for Fe_2O_3-MnO_2 and Fe_2O_3-Mn_2O_3 systems, and X_{Co} = 42.0% and 12.0%, for Co_3O_4-MnO_2 and Co_3O_4-Mn_2O_3 ones.

Secondary ion mass spectrometry (SIMS) analyses were carried out by means of an IMS 4f mass spectrometer (Cameca) using a 14.5 keV Cs^+ primary beam (25 nA, stability = 0.3%), rastering over a 150×150 μm^2 area and collecting negative secondary ions from a 7×7 μm^2 sub-region. Measurements were carried out in high mass resolution configuration and beam blanking mode, using an electron gun for charge compensation. The sputtering time in the profile abscissa was converted into depth basing on deposit thickness values measured by field emission-scanning electron microscopy (FE-SEM) analyses. The latter were performed using a Zeiss SUPRA 40VP instrument, at a primary beam voltage of 10 kV. The mean nanoaggregate dimensions were evaluated using the ImageJ® software.

Atomic force microscopy (AFM) micrographs were collected using an NT-MDT SPM Solver P47H-PRO instrumentation, operating in semi-contact mode and in air. Root mean square (RMS) roughness values were calculated after image processing through background subtraction and plane fitting, at a window size of 5×5 μm^2.

X-ray diffraction (XRD) patterns were collected using a Bruker D8 Advance diffractometer equipped with a CuKα X-ray source ($\lambda = 1.54051$ Å) and a Göbel mirror, at an incidence angle of 1.0°.

Thin cross-sectional samples for transmission electron microscopy (TEM) analyses were prepared using Helios 450s FIB/SEM (Thermo Fisher, USA) *via* a standard protocol by means of focused ion beam (FIB) technique. Pre-thinned lamellas were lifted out from the target specimen, attached to TEM grid and subsequently thinned down to electron transparency. Final cleaning was performed with FIB operating at 5 kV and 25 pA. Whenever necessary, a protective platinum layer was deposited during sample preparation to embed the structures and prevent them from collapsing. TEM analyses, including high resolution TEM (HRTEM), high-angle annular dark-field scanning TEM (HAADF-STEM), and energy dispersive X-ray spectroscopy (EDXS) elemental mapping of Mn_2O_3-based electrodes were carried out on a double aberration corrected JEM ARM200F (200 kV) cold FEG microscope, equipped with a

9

large solid angle CENTURIO EDX detector, Orius CCD camera and Quantum GIF. The EDXS mapping of MnO_2-based specimens was performed using a FEI Titan[3] (300 kV) microscope using a 4-detector large angle Super X setup.

2.3 Electrochemical studies

Electrochemical tests were carried out at room temperature (20°C) by an electrochemical working station (VMP3, BioLogic Science Instruments) using a three-electrode set-up (see Scheme 1). The FTO-supported manganese oxide-based systems were used as WEs, whereas a Pt mesh was used as CE. Despite the use of a carbon-based counter-electrode could, in principle, be convenient, in the present case the issue is less severe since the working electrode is an anode, and Pt dissolution under cathodic polarization is less prone to happen, according to the electrode potential-pH diagram (Pourbaix diagram) [55]. A Hg/HgO (MMO) electrode, typically employed in alkaline media, was selected as the reference (RE). The inner RE solution was regularly changed in order to avoid any undesired degradation due to Cl⁻ presence in the reaction medium, and the RE potential was often checked against a lab electrode in order to ensure a full reproducibility of the results obtained in repeated experiments. The obtained currents were normalized to the electrode geometric area (≈ 1.0 cm^2). Electrochemical tests were initially performed in an alkaline-simulated seawater electrolyte (0.5 M KOH + 0.5 M NaCl) [28], and subsequently in Mediterranean seawater picked up at the seaside of Barcelona (Spain). The latter was used as an electrolyte after adding KOH and filtering the precipitate (mainly formed by Mg hydroxide; final *pH* = 13.5). The potential was converted into the reversible hydrogen electrode (RHE) scale by the relation [8,29,33,56]:

$$E_{RHE}(V) = E_{MMO}(V) + 0.059 \times pH + 0.111 \tag{3}$$

The data presented for the electrochemical characterization do not include compensation for the series resistance of the solution. The overpotential for oxygen evolution (η) was computed

using the formula [8,16-17,33,57]:

$$\eta \ (V) = E_{measured} \ (V \ vs. \ RHE) - 1.23 \tag{4}$$

where $E_{measured}$ and 1.23 are the experimental potential and the $E°$ value for O_2 evolution $vs.$ RHE, respectively.

Linear sweep voltammetry (LSV) measurements were performed at a scan rate of $1 \ mV \times s^{-1}$. Tafel slopes were calculated using polarization curves by plotting potential against log(current density). Chronoamperometry (CA) analyses were carried out for 1 h at 1.94 V ($vs.$ RHE), $i.e.$ in a potential range that does not prevent hypochlorite generation ($\eta = 0.71 \ V > 0.48 \ V$) [14,16,31-32]. The O_2 amount produced during OER was monitored by headspace gas analysis using a fiber optic trace oxygen transmitter (Fibox 3 trace v3), and subsequently used to evaluate the OER Faradaic efficiency (see the Supporting Information). The O_2 probe was inserted in the electrochemical compartment through a tightly sealed septum, and continuous readings of O_2 partial pressure were performed throughout each experiment. Prior each measurement, oxygen from air was removed by fluxing N_2 into the reaction medium. Immediately after CA experiments, iodide titration was used for the determination of hypochlorite species generated during OER (see the Supporting Information).

3. Results and Discussion

3.1. Characterization of MnO_2 and Mn_2O_3-based electrodes

To obtain an insight into the chemical composition of the fabricated electrode materials as a function of the adopted processing conditions, XPS analyses were employed. For all specimens, Mn photoelectron peaks were well detectable (Fig. 1a-b; Fig. S1a-b), suggesting a high dispersion of Fe- and Co-containing species into the pristine manganese oxides. For samples subjected to annealing in air (see Scheme 1), the Mn2p peak shape and position confirmed the obtainment of pure MnO_2 (Fig. 1a; BE(Mn2p$_{3/2}$) = 642.6 eV) [3,25,51-52,58].

11

The presence of Mn(IV) oxide was further supported by two important fingerprints of Mn oxidation state, the Mn3s multiplet splitting separation (4.6 eV, Fig. S1a) [3,16,19,53] and by the BE difference (Δ) between the $Mn2p_{3/2}$ and O1s lattice components (see below; $\Delta = 112.6$ eV) [24,44,51].
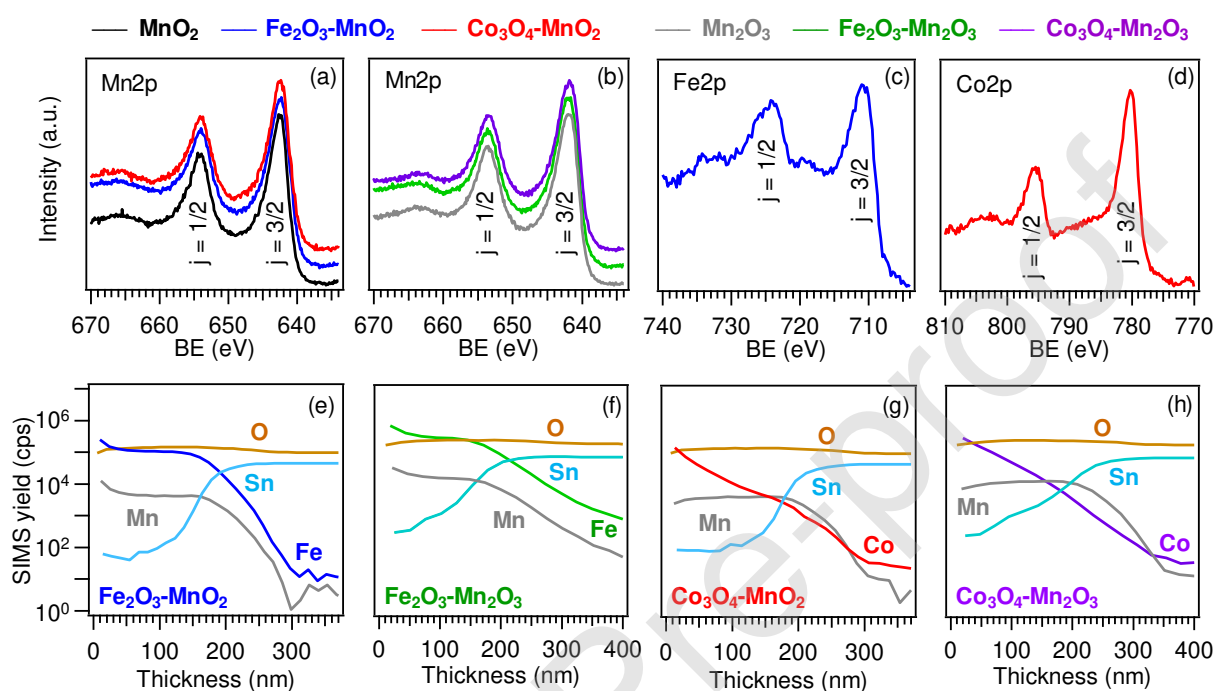

Figure 1. (a-d) XPS analysis of as-prepared specimens: Mn2p photoelectron peaks for MnO_2- (a) and Mn_2O_3- (b) based electrodes; (c) Fe2p and (d) Co2p signals for Fe_2O_3-MnO_2 and Co_3O_4-MnO_2 samples. SIMS depth profiles for Fe_2O_3-MnO_2 (e), Fe_2O_3-Mn_2O_3 (f), Co_3O_4-MnO_2 (g), Co_3O_4-Mn_2O_3 (h).

In a different way, thermal treatments under Ar (see Scheme 1) resulted in the selective formation of Mn_2O_3 (Fig. 1b; $BE(Mn2p_{3/2}) = 641.9$ eV, $BE(Mn2p_{1/2}) = 653.5$ eV) [16,18,22,33], as confirmed also by the Mn3s component separation (5.4 eV, Fig. S1b) [35,43,47] and by a Δ value of 111.8 eV [24,50]. For both kind of systems, the Fe2p (Fig, 1c and S1c; $BE(Fe2p_{3/2}) = 711.0$ eV) and Co2p (Fig. 1d and S1d; $BE(Co2p_{3/2}) = 780.2$ eV) photoelectron peaks were consistent with the occurrence of pure Fe_2O_3 [15,44,59] and Co_3O_4 [11,54]. The presence of the latter was further corroborated by the cobalt Auger parameter ($\alpha = 1552.7$ eV) [49,54], and by the absence of *shake-up* satellites [22-23]. Taken together, these results highlighted the

12

formation of nanocomposite systems in which both the pristine manganese oxides and Fe_2O_3/Co_3O_4 maintained their chemical identity. For all samples, the O1s photoelectron peak (Fig. S2) resulted from the contribution of two components at mean BE values of 530.0 eV (I) and 531.7 eV (II), attributable to lattice oxygen (I) and to hydroxyl groups/oxygen species chemisorbed on surface O defects (II) [11,48,51-52,54]. The occurrence of the latter was also supported by optical absorption analyses (see Fig. S3 and related comments). As indicated in the caption for Fig. S2, component (II) underwent an increase with respect to the (I) on going from bare manganese oxides to functionalized systems. Since an increased oxygen defect content promotes a higher reactivity, the above phenomenon is deemed to enhance the functional performances of composite electrodes with respect to the pristine Mn oxides [3,33,41,48].

Additional information on material in-depth composition was gained by SIMS profiling (Fig. 1e-h and S4). The obtained results indicated a good purity of all the developed systems, as testified by an estimated mean C concentration lower than 75 ppm. Irrespective of the processing conditions, the O ionic yield remained constant throughout the investigated depth and the tailing of tin from the substrate into the deposits suggested the occurrence of Sn diffusion triggered by thermal treatments [15]. This phenomenon, already observed in previous works using FTO as supporting electrode material, might beneficially influence electrochemical performances, thanks to an improved electrical conductivity [49].

As concerns Fe_2O_3-containing samples (Fig. 1e-f), iron and manganese curves displayed a parallel trend, indicating an even in-depth composition and effective iron oxide dispersion within the pristine MnO_2/Mn_2O_3 network. This phenomenon, ascribed to the concurrent contribution of manganese oxide open structure and the inherent RF-sputtering infiltration power [49], was further boosted by the performed thermal treatment. The resulting intimate contact between MnO_2/Mn_2O_3 and Fe_2O_3 particles enables indeed to exploit their mutual interplay for the target applications (see below). Regarding Co_3O_4-containing materials (Fig.

13

1g-h), the outermost sample regions were Co-rich, as clearly shown by a comparison of Mn and Co yields *vs*. depth. In particular, the cobalt signal underwent a progressive decrease at higher depth values, indicating that Co_3O_4 was more concentrated in the near surface regions and less efficiently dispersed into the inner ones (see also TEM and EDXS analyses). This phenomenon may directly affect the electrocatalytic activity of the manufactured systems, as discussed below.
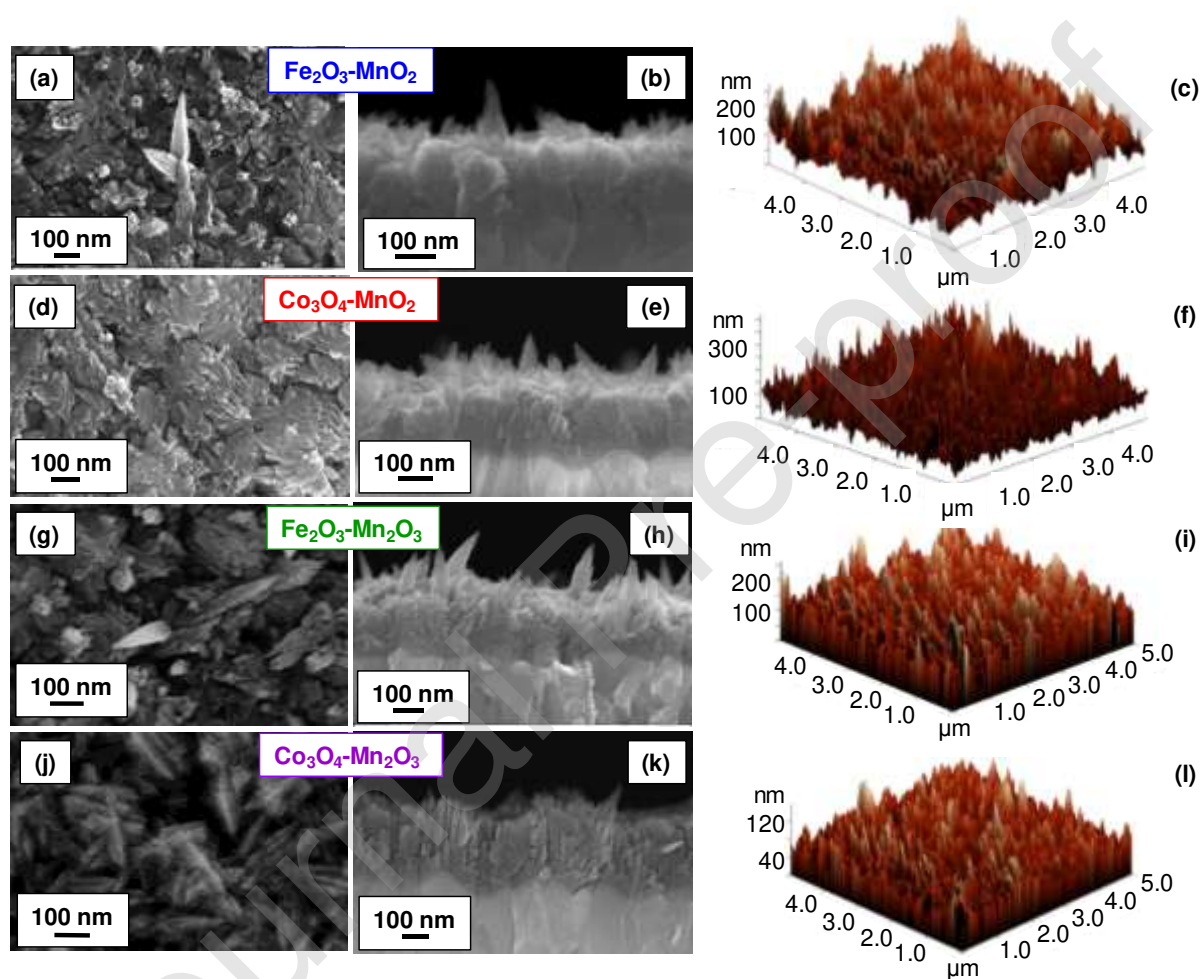

Figure 2. (From left to right) Plane-view, cross-sectional FE-SEM images and AFM micrographs for MnO_2 and Mn_2O_3 samples functionalized with Fe_2O_3 and Co_3O_4.

Subsequently, efforts were dedicated to the investigation of material morphology by FE-SEM and AFM. Both bare MnO_2 and Mn_2O_3 (mean deposit thickness = 300±40 nm (MnO_2, Fig. S5a-b) and 270±30 nm (Mn_2O_3, Fig. S5d-e)) were characterized by an inherently open nano-organization, an important starting point to achieve the dispersion of the over-deposited

Fe_2O_3 and Co_3O_4. In the case of MnO_2, sparse quasi-1D pointed nanoaggregates (mean length = 150±40 nm), protruding from a more compact granular underlayer, could be clearly observed. As concerns Mn_2O_3, the recorded micrographs displayed the presence of lamellar structures (length = 120±40 nm), whose interconnection produced larger dendritic assemblies. For both kinds of systems, the subsequent RF-sputtering of Fe_2O_3 and Co_3O_4 (Fig. 2) resulted in the occurrence of modest morphological variations, corresponding to the formation of more rounded aggregate features. Irrespective of the adopted processing conditions, AFM images (Fig. S5c and f, and Fig. 2c,f,i,l) indicated the occurrence of multigrain structures, in line with FE-SEM observations. The obtained root-mean-square (RMS) roughness values ($\approx$ 35 nm and 25 nm for the MnO_2- and Mn_2O_3-based nanosystems, respectively) suggested an appreciable active area [51,53], favorably affecting the eventual electrochemical performances [3,11,16,48].

Preliminary structural analyses by XRD evidenced diffraction peaks corresponding to β-MnO_2 (Fig. S6a; 2θ = 28.7°, (110); 2θ = 37.4°, (101)) [60], for air-annealed samples, and of β-Mn_2O_3 (Fig. S6b; 2θ = 23.2°, (211); 2θ = 33.1°, (222); 2θ = 38.3°, (400)) [61], for Ar-annealed ones. The relatively low diffracted intensity, along with the relatively large peak width, suggested the formation of small and defective nanocrystallites [23,51,53], in line with TEM and XPS results. Upon functionalization by RF-sputtering, no appreciable signals related to Fe or Co oxides could be detected, a phenomenon due to their relatively low amount and/or small crystallite sizes, as well as to their dispersion into the pristine MnO_2/Mn_2O_3 systems [15,49]. In addition, no diffraction peaks related to Mn-Fe-O or Mn-Co-O ternary phases could be clearly observed. Nevertheless, an apparent decrease of the overall diffracted intensity after RF-sputtering was observed and attributed to plasma-surface interactions and ion bombardment of Mn oxides upon Fe_2O_3 or Co_3O_4 deposition [52-53]. This phenomenon was responsible for an increase in the O defect content upon going from the pristine MnO_2 and Mn_2O_3 to Co_3O_4- and Fe_2O_3- containing materials (see above and Fig. S2).
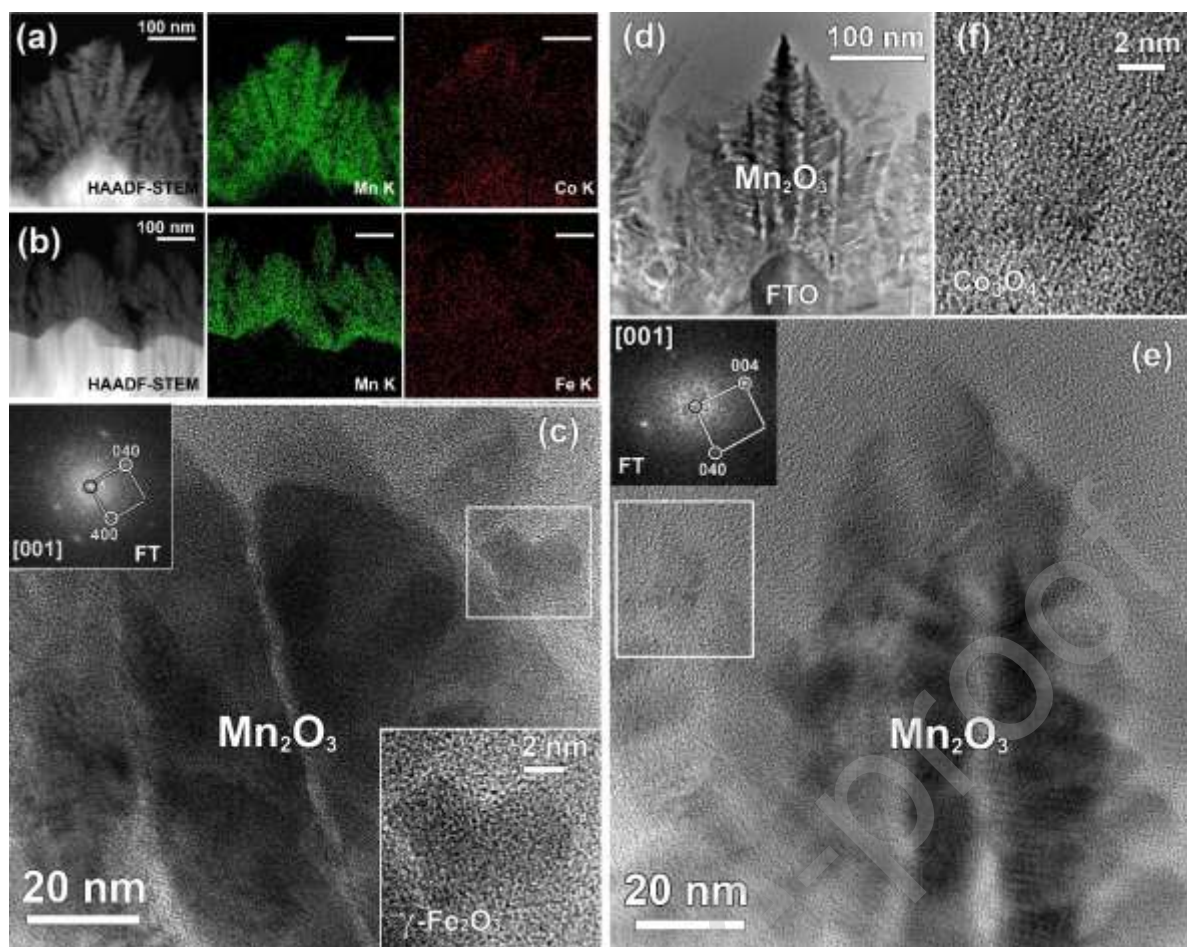
15

Figure 3. (a,b) HAADF-STEM images and corresponding EDXS elemental mapping of MnK and CoK lines for Mn_2O_3 specimens functionalized with (a) Co_3O_4 and (b) Fe_2O_3. (c) Bright field HRTEM image for a Mn_2O_3 specimen functionalized with Fe_2O_3. The white box marks a single Fe_2O_3 nanoparticle, whose enlargement is given as inset. The corresponding FT pattern ([001] zone axis) in the upper left corner of Fig. 3c reveals the occurrence of the cubic γ-Fe_2O_3 polymorph. (d) Low magnification bright field TEM and (e) HRTEM images of a Mn_2O_3 sample functionalized with Co_3O_4. The white box marks a single Co_3O_4 nanoparticle (enlargement given in (f)). The corresponding FT pattern ([001] zone axis) in the top left corner of Fig. 3e indicates the presence of cubic Co_3O_4.

To gain a deeper insight into the nanoscale structure of the present systems, TEM analyses were undertaken on functionalized specimens (Fig. 3). Due to the inherent roughness of the FTO substrate, the Mn_2O_3 deposit was characterized by the assembly of irregular dendritic structures into high area arrays (Fig. 3a,b,d), as already evidenced by FE-SEM investigation (see above). EDXS chemical maps in Fig. 3a-b confirmed the successful functionalization of Mn_2O_3 surface with cobalt and iron oxide nanoparticles. Due to the relatively small amount of the latter, the pertaining Co and Fe EDXS signals were rather weak, though still detectable

16

thanks to the use of a large angle, high sensitivity EDXS detector.

A careful inspection of the maps reveals that, despite both Co-and Fe-containing oxides were dispersed over the entire dendrite-like structures, the former was more concentrated in the near-surface regions, in accordance with the above presented SIMS data. An analogous spatial distribution of functionalizing agents was observed in the case of MnO_2-based specimens (see Fig. S7 and related comments). A careful analysis of HRTEM images (Fig. 3c-e) enabled to gain information on the structure of iron and cobalt oxide nanoparticles. The inset of Fig. 3c displays a HRTEM image of a single iron oxide nanoparticle, having a mean size of ≈ 8 nm, whose structure corresponded to that of the cubic γ-Fe_2O_3 (*maghemite*) polymorph [62] (see the Fourier transform (FT) pattern in the inset of Fig. 3c). The formation of this iron(III) oxide polymorph, instead of the most thermodynamically stable one α-Fe_2O_3 (*hematite*), was traced back to the non-equilibrium plasma conditions characterizing RF-sputtering [49]. The FT analysis of cobalt oxide nanoparticle HRTEM images (Fig. 3f, mean dimensions ≈ 4 nm) evidenced the presence of cubic Co_3O_4 (Fig. 3e, inset) [63]. No ternary Mn-Fe-O or Mn-Co-O phases could be detected, in line with XRD results.

3.2. Catalytic activity of MnO_2 and Mn_2O_3-based electrodes in simulated and natural seawater

The system electrochemical performances were first studied in simulated seawater (0.5 M KOH + 0.5 M NaCl). Linear sweep voltammetry curves pertaining to MnO_2- and Mn_2O_3-based materials (Fig. 4a-b, respectively) evidenced the beneficial Fe_2O_3 and Co_3O_4 role, since all composites showed higher current densities and lower η values than bare MnO_2 or Mn_2O_3 (Fig. 4c-d and Table S1). As can be observed, bare Fe_2O_3 and Co_3O_4 yielded appreciably lower current densities than all the other investigated systems.

To the best of our knowledge, the electrocatalytic activities of MnO_2 and Mn_2O_3, as well those of the corresponding composite systems, expressed in terms of overpotential, current

density at fixed potentials, and Tafel slope values (Table S1), are better than those reported in previous studies for various manganese oxide-based systems, including MnO_2 [45], Mn_2O_3 [46], WO_3-Mn_2O_3 [47], $(Mn$-$Mo)O_x$/IrO_2/Ti [64] and $(Mn$-Mo-$W)O_x$/IrO_2/Ti [65].
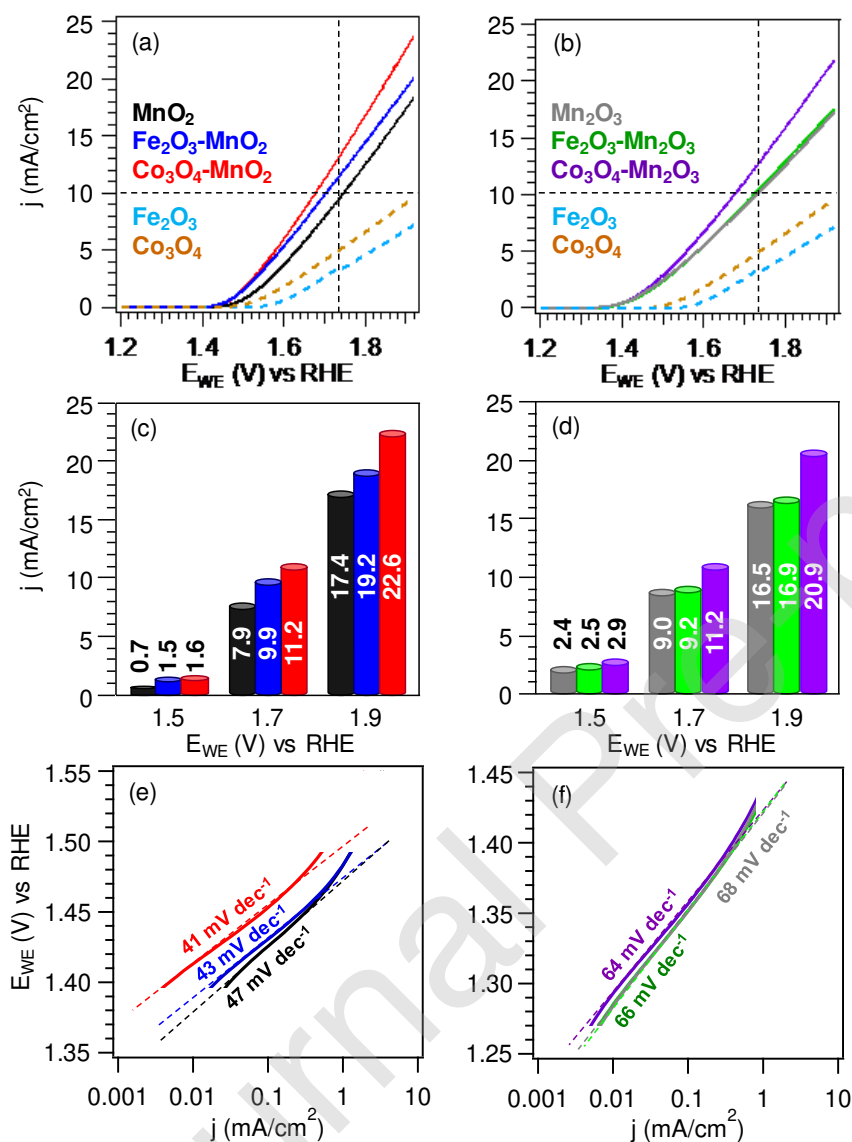

Figure 4. OER performances of manganese oxide-based electrodes in simulated alkaline seawater. (a,b). LSV curves. In (a-b), Fe_2O_3 and Co_3O_4 curves are also reported for comparison. Vertical and horizontal dashed lines indicate η = 500 mV and j = 10 mA×cm^{-2}, respectively. Current densities at different potentials (c,d) and Tafel plots (e,f) for MnO_2- and Mn_2O_3-based electrodes. Continuous and dashed lines indicate experimental and fitting curves, respectively.

The performance enhancement observed in composite systems could be traced back to the concurrent contribution of different phenomena: i) the intrinsic catalytic activity of Fe and Co oxides towards OER [5,7,22,35,48-49,57,66]; ii) the higher oxygen defect content (see XPS

data) [3,33,41,48]; iii) the formation of oxide/oxide heterojunctions, yielding an improved charge carrier separation [67]. Further details regarding the role of Fe_2O_3 and Co_3O_4 on the overall activity and a possible rationale for the higher performances of Co_3O_4-containing systems are discussed in more detail below. The Tafel slope values (Fig. 4e-f; Table S1) suggested a higher catalytic activity for MnO_2-based materials, since these systems showed a slope $\approx$20 mV/decade lower than the homologous Mn_2O_3-based ones [5,17,23,48].

A detailed analysis of Fig. 4c-d revealed that MnO_2-based materials exhibited lower current densities than Mn_2O_3-based ones at low potential values, whereas the opposite held for potentials higher than $\approx$ 1.8 V *vs.* RHE. Pokhrel *et al.* [42] evidenced that Mn_2O_3 activity outperformed all the others manganese oxides in HNO_3 solution (0.1 M; pH = 1), whereas MnO_2 showed the highest activity in NaOH solution (0.1 M; pH = 13). The higher catalytic activity of MnO_2-based electrodes could be explained by considering the different composition of simulated seawater and freshwater, that have a significant influence on the resulting performances [56,68].

Preliminary CA measurements (Fig. 5a-b) evidenced that, after an initial transient period ($\approx$ 5 min), all the target materials exhibited a good stability for a total test time of 1 h. In particular, bare MnO_2 resulted to be more stable than Mn_2O_3 (j loss = 3.9% and 4.4% for MnO_2 and Mn_2O_3, respectively) and, in both cases, the introduction of Co_3O_4 enhanced the system stability, resulting in a lower j decrease (Table S2). In order to attain a deeper insight into the system long-term stability, CA experiments were repeated up to a total duration of 24 h (one day) for all the surface-decorated MnO_2- and Mn_2O_3-based electrodes. The obtained curves are displayed in Fig. S8. As can be observed, after an initial current decrease, all the target electrodes exhibited a good stability upon a more prolonged utilization. This important pre-requisite paves the way to the eventual practical utilization of manganese oxide composite electrodes in real-world devices (see also the comments below).

In order to evaluate OER selectivity, the amount of O_2 produced during OER was measured
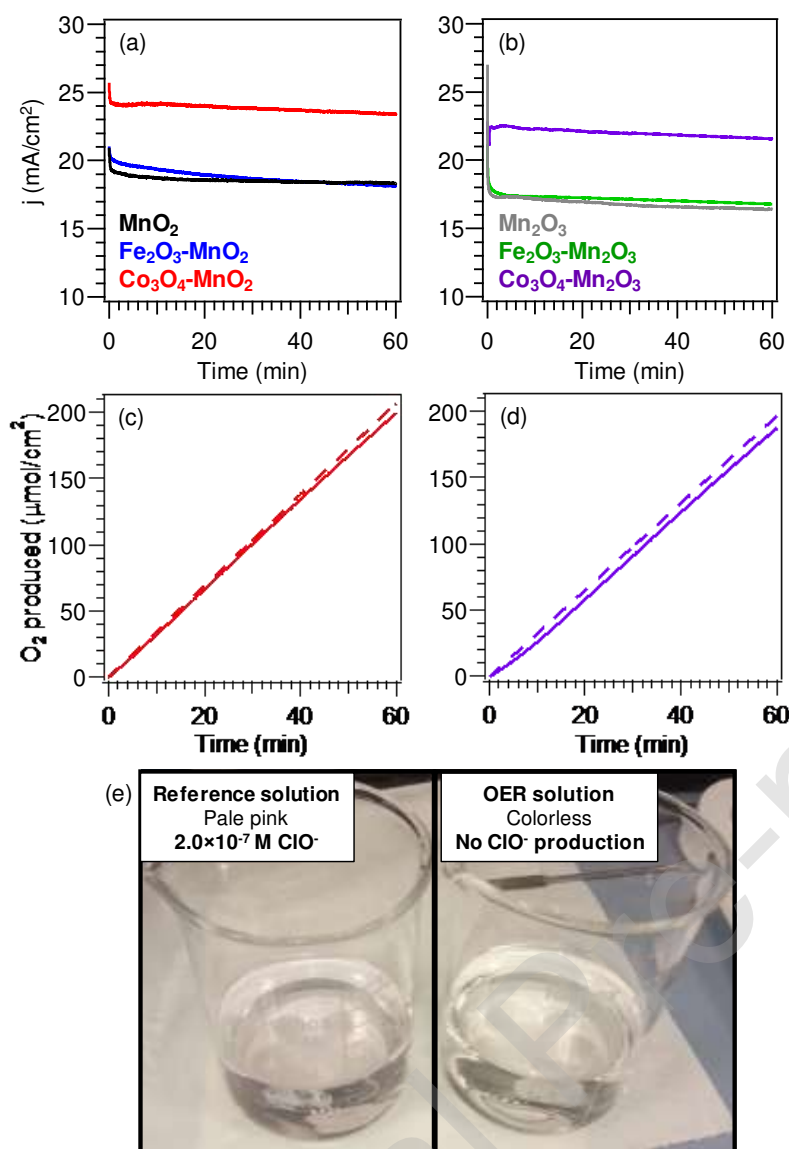
Figure 5. (a,b) Chronoamperometry of MnO_2- and Mn_2O_3-based electrodes in the OER in simulated alkaline seawater (fixed potential of 1.94 V *vs*. RHE). (c,d) O_2 evolution rate measured over 60 min for the best-performing samples in (a) and (b). Continuous and dashed lines mark experimental and theoretical curves (calculated assuming 100% efficiency), respectively. (e) Digital photographs of the reference and OER solutions for the iodometric titration, showing the absence of ClO^- production in the latter case.

as a function of time. Fig. 5c-d display the results obtained for the best performing samples, *i.e.*

Co_3O_4-MnO_2 and Co_3O_4-Mn_2O_3 (see Fig. S9 for the other specimens). Interestingly, both

materials yielded a Faradaic efficiency close to 100% (see also Table S2), and a total generated

O_2 amount of 200 and 190 $\mu mol \times cm^{-2}$ for Co_3O_4-MnO_2 and Co_3O_4-Mn_2O_3 specimens,

respectively. Iodometric titration data (Supporting Information) clearly indicated the absence

of any hypochlorite trace (compare the pale pink color of reference solution and colorless OER

20

solution in Fig. 5e), thus confirming the OER selectivity of the tested systems. This result enabled to exclude that current density variations with time could be induced by corrosive ClO$^-$ species, a favorable issue for the eventual applications of the manufactured electrodes.

Basing on the promising results obtained in simulated seawater, all materials were subsequently tested as OER anodes in Mediterranean alkaline seawater. In general, all the key performance indicators (η at 10 mA×cm^{-2}, j at 1.73 V $vs.$ RHE, and Tafel slope) were inferior than the corresponding ones obtained in simulated seawater (compare Tables S3 and S1). This phenomenon, in line with previous studies [14,28], could be likely ascribed to the occurrence of impurities in real seawater [29], as well as to the higher ionic strength of Mediterranean alkaline seawater in comparison to the artificial alkaline homologous. In fact, this phenomenon decreases the local availability of H_2O molecules required for OER at the electrode/electrolyte interface, decreasing thus the resulting O_2 evolution rate [36]. In agreement with the above results, LSV curves (Fig. 6a-b) evidenced the beneficial role exerted by Fe_2O_3 and Co_3O_4 functionalization. In addition, Tafel slope values (Fig. S10 and Table S3) confirmed the higher catalytic activity of MnO_2-based materials, as already observed for OER in artificial seawater. CA curves (Fig. 6c-d) highlighted a good stability for all the investigated systems after an initial period of ≈10 min. However, current density loss over time resulted higher than the one observed in artificial seawater, a direct consequence of the more complex seawater composition and of the already mentioned impurities presence [29].

Fig. 6e-f report the O_2 amount produced throughout 1 h of chronoamperometry at 1.94 V $vs.$ RHE and the corresponding theoretical one for the best-performing Co_3O_4-containing samples. These data indicated a Faradaic efficiency close to 100% (see Table S4), as already observed in the case of artificial seawater, validating thus the selectivity towards OER even in natural seawater. An analogous behavior was exhibited by all the other samples (see Fig. S11). To attain additional information on the stability of the present materials, the target systems were stored at room temperature in air for six months and tested as OER anodes every 90 days. The

obtained results (Fig. S12) revealed no significant current density variations, evidencing a good

stability of the target anodes. This issue, further corroborated by XPS measurements performed

after six months of electrochemical tests (Fig. S13; compare with Fig. 1a and d and Fig. S1 and

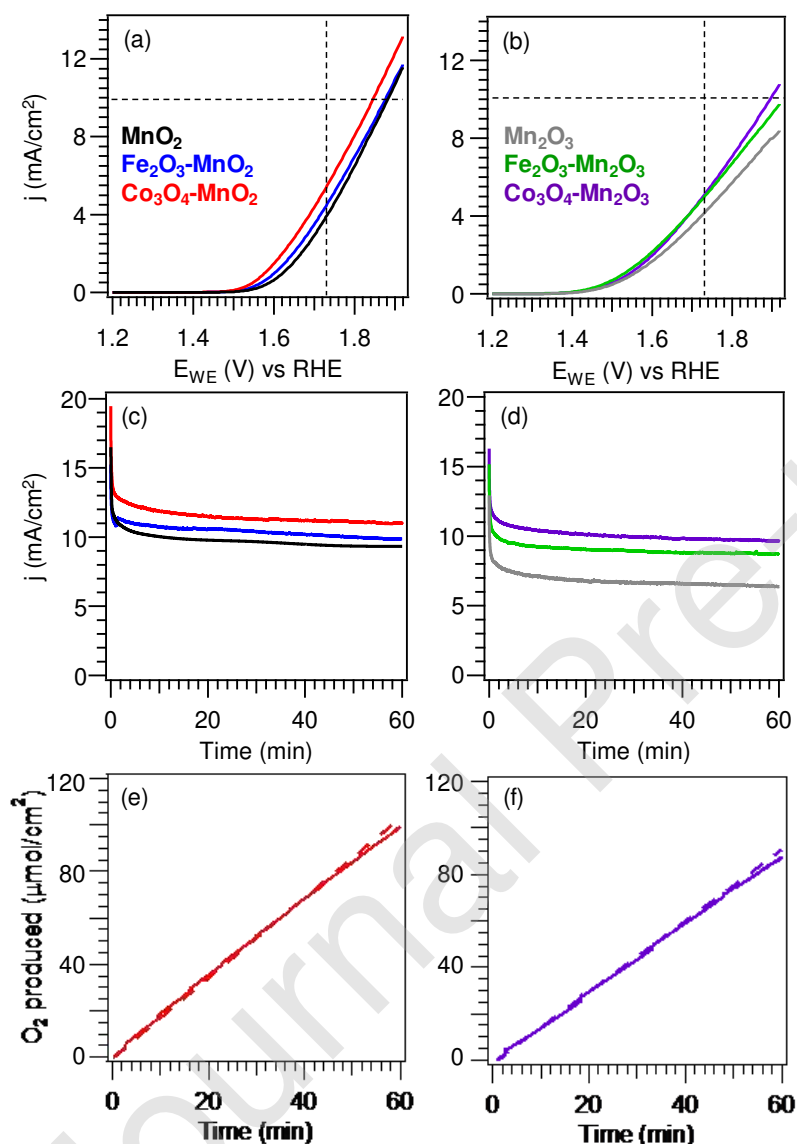S2), enabled to rule out a significant material dissolution/degradation.

Figure 6. Electrochemical OER performances of manganese oxide-based electrodes in Mediterranean alkaline seawater. (a,b) LSV curves. Vertical and horizontal dashed lines indicate η = 500 mV and j = 10 mA×cm^{-2}, respectively. (c,d) Chronoamperometry of MnO_2- and Mn_2O_3-based electrodes. (e,f) O_2 evolution rate per unit area measured over 60 min for the best-performing Co_3O_4-containing samples in (a) and (b). Continuous and dashed lines indicate the experimental and theoretical curves, respectively.

As a matter of fact, the occurrence of surface reconstruction phenomena under

electrochemical conditions has been reported in the literature for MnO_2- and Mn_2O_3-based materials [69-72]. In general, surface reconstruction can involve morphological, structural and electronic alterations in manganese oxides, as well as variations of Mn valence state and generation of surface defects, appreciably influencing the ultimate system electrochemical performances [69-72]. However, in this work, the experimental data reported in Fig. S8, S12 and S13 reveal a good operational stability of all manganese oxide composite electrodes, suggesting that surface reconstruction phenomena have a modest effect in the present case.

Taken together, the experimental results discussed so far highlight the positive effect exerted by manganese oxide functionalization with iron and cobalt oxides on the ultimate OER performances. To date, different works have investigated the electrocatalytic activity of iron and cobalt oxides, in particular Fe_2O_3 and Co_3O_4 [5,7,22,35,48-49,57,66], and the latter has been reported to yield higher OER performances than the former, in line with the well-known Co_3O_4 functional activity as heterogeneous catalyst in a variety of oxidation reactions [5-7,21,66]. Nevertheless, other studies highlighted that the functionalization/doping with Fe, instead of Co, resulted in a higher activity enhancement of the resulting composite material [8,27,66]. The question that now raises is: why does Co_3O_4 introduction result in a higher performance enhancement with respect to the case of Fe_2O_3? The answer is based on the concurrent contribution of catalytic, and electronic effects, as well as on the influence of Fe_2O_3 or Co_3O_4 in-depth spatial distribution. In this regard, Fig. 7 proposes a rational mechanism based on the results collected through the multi-technique characterization performed in the present work. The green square contains a sketch of the catalytic effect, in which the arrow thickness is proportional to the current density produced at a specific reaction site. In particular, the thin yellow arrow marks electrons originating during OER from bare MnO_2 or Mn_2O_3, whereas the homologous thick one indicates electrons produced by composite materials. As anticipated, another concurrent phenomenon contributing to the material activity is the formation of heterojunctions between the pristine oxide (MnO_2 or Mn_2O_3) and the

23

functionalizing agents (Fe_2O_3 or Co_3O_4), resulting in an improved separation of charge carriers and in a higher OER activity (electronic effect, blue square in Fig. 7). At the *p-n* heterojunctions (Co_3O_4/MnO_2 and Co_3O_4/Mn_2O_3), electrons in MnO_2 or Mn_2O_3 (*n*-type semiconductor) will flow to Co_3O_4 (*p*-type semiconductor) [67]. In a different way, at *n-n* heterojunctions (Fe_2O_3/MnO_2 and Fe_2O_3/Mn_2O_3), electrons will flow from the higher energy conduction band of MnO_2 or Mn_2O_3 to the lower- energy one (Fe_2O_3) [67].
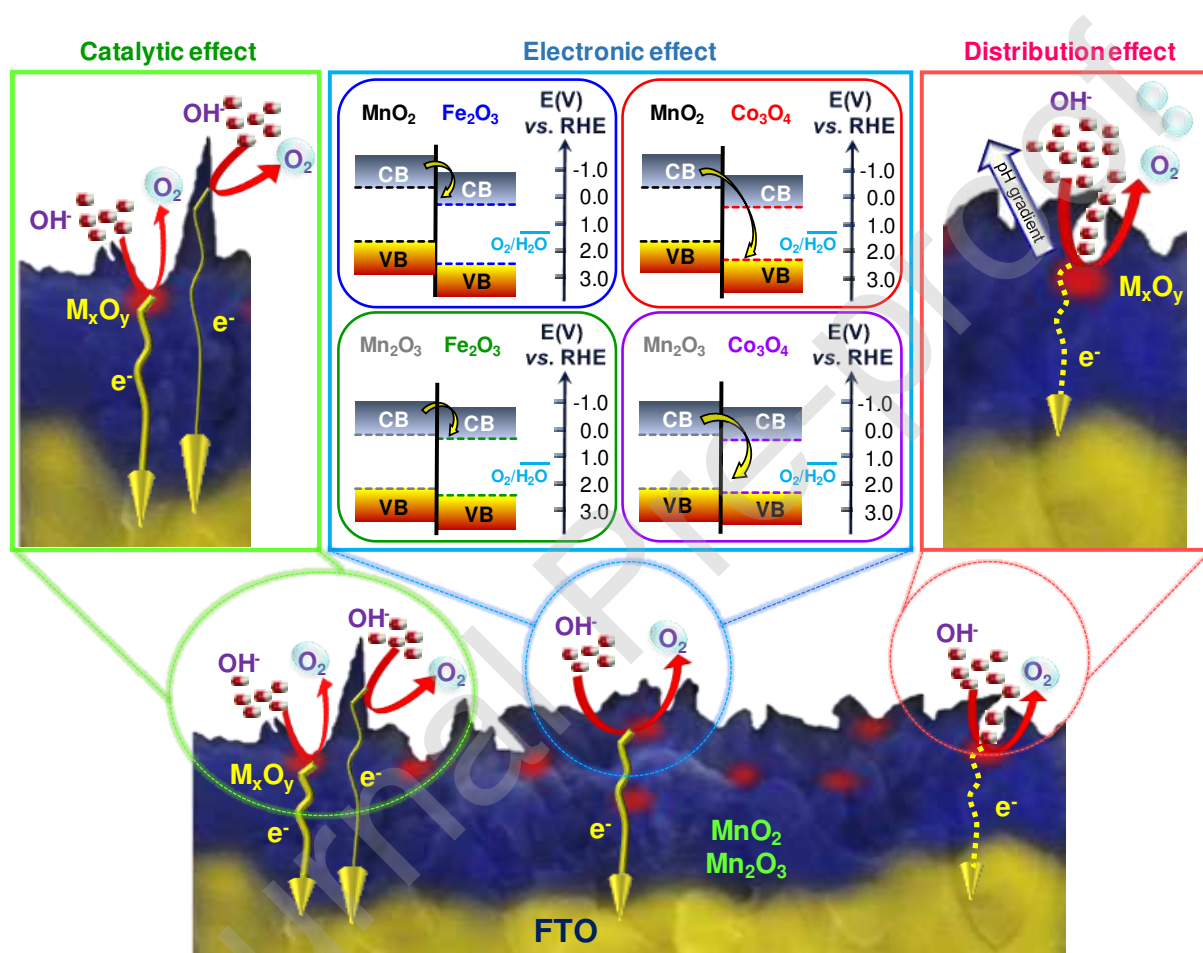

Figure 7. Sketch of the concurring effects accounting for the different OER performances of MnO_2- and Mn_2O_3-based electrodes. M_xO_y = Fe_2O_3, Co_3O_4. The central panel contains a schematic energy band diagram of Fe_2O_3-MnO_2, Co_3O_4-MnO_2, Fe_2O_3-Mn_2O_3 and Co_3O_4-Mn_2O_3 systems, with approximate energy levels with respect to the RHE scale [53,59,73-74]. CB and VB mark the conduction and valence bands, respectively.

These phenomena are expected to be enhanced for Co_3O_4/MnO_2 and Co_3O_4/Mn_2O_3 heterojunctions in comparison to the homologous Fe_2O_3/MnO_2 and Fe_2O_3/Mn_2O_3 ones, due to the higher energy difference (ΔE_B; Tables S5 and S6) between Co_3O_4 VB and manganese

oxides CB [67]. It is worthwhile observing that ΔE_B values for MnO_2-based composites are higher than for Mn_2O_3-based ones. The above explanation could account for: i) the enhanced OER performances produced by functionalization with Co_3O_4, rather than Fe_2O_3; ii) the higher current densities and lower Tafel slopes for MnO_2-based composites in comparison to Mn_2O_3-based ones. A further contributing effect can be related to the different in-depth distribution of Fe_2O_3 and Co_3O_4 in the pristine manganese oxides (distribution effect in Fig. 7). As evidenced by SIMS analyses (see above), Fe_2O_3 was evenly dispersed into MnO_2 and Mn_2O_3 (Fig. 1e-f), whereas Co_3O_4 was more concentrated in the near surface regions of both manganese oxides (Fig. 1g-h). In general, a higher in-depth dispersion (as for Fe_2O_3-containing specimens), and the resulting intimate contact between Fe_2O_3 and MnO_2/Mn_2O_3, can boost the system activity thanks to the higher heterojunctions number and the reduced charge carrier transport distance to the external circuit. On the other hand, an enhanced in-depth dispersion may prevent an efficient diffusion and mixing of the reactant species in solution, especially at the less accessible active sites, such as those located at grain boundaries (see the red M_xO_y nanoparticle in the orange square in Fig. 7) [56]. This effect, in turn, results in the formation of *pH* gradients around Fe_2O_3 nanoparticles during OER process [75]. As a matter of fact, the *pH* value has a direct influence on aqueous electrochemical processes, and previous studies have shown that *pH* variations of different units can occur near the electrode surface with respect to bulk seawater [4,9,75]. In particular, OER activity of oxides materials increases at higher *pH* values [31,76]. As a consequence, the catalytic activity and in-depth dispersion of Fe_2O_3 may be likely counterbalanced by the *pH* decrease, reducing thus the OER activity of Fe_2O_3 containing samples (see the yellow dashed line in Fig. 7). In conclusion, the synergistical combination of these effects provides a reasonable explanation for the higher electrocatalytic enhancement yielded by the introduction of Co_3O_4, rather than Fe_2O_3. The underlying reasons can be summarized as follows: i) the intrinsic catalytic activity of Co_3O_4 is higher than that of Fe_2O_3 (see above); ii) oxide-oxide heterojunctions at the interface between Co_3O_4 and MnO_2/Mn_2O_3

are more proficient in enhancing charge carrier separation than the ones obtained with Fe_2O_3; iii) the more pronounced concentration of Co_3O_4 in the near-surface regions with respect to Fe_2O_3 reduces *pH* gradient effects. In addition, the higher ΔE_B of MnO_2 composites with respect to the Mn_2O_3 homologues (Table S6) may explain the higher OER activity of MnO_2 composites with respect to Mn_2O_3 ones.

3. Conclusions

In this work, MnO_2 and Mn_2O_3 nanocomposites, functionalized with Fe_2O_3 or Co_3O_4, as anodes for seawater splitting were fabricated by an original plasma-assisted process. After the initial growth of manganese oxides on FTO by PE-CVD, Fe_2O_3 and Co_3O_4 were introduced by RF-sputtering. The final thermal treatment in air or inert atmospheres yielded phase-pure MnO_2- or Mn_2O_3-based systems, endowed with a high active area, an inherent oxygen defectivity, and an intimate contact between MnO_2/Mn_2O_3 and the introduced Fe_2O_3 and Co_3O_4. The proposed plasma-assisted procedure turned out to be versatile and powerful in the preparation of advanced anodes for saline water splitting, with performances higher than the pristine manganese oxides. Among the various options, Co_3O_4-MnO_2 was assessed as the most appealing one, with an outstanding Tafel slope of ≈ 40 mV$\times$dec^{-1}, current densities up to ≈ 13 mA$\times$cm^{-2} and an overpotential of 450 mV, below the hypochlorite formation threshold corresponding to 480 mV. The present systems stand as highly selective anodes for O_2 generation from seawater, a largely available natural resource, avoiding at the same time chloride-induced corrosion. The resulting electrocatalytic activities, rationalized in terms of the electronic and catalytic interplay between the single oxide constituents, were accompanied by an attractive durability in alkaline environments. The proposed material combinations open the door to the eventual implementation of electrodes for use in cost-effective devices enabling H_2 production from seawater, facilitating hydrogen integration in the energy models of a decarbonized and sustainable society. In perspective, a computational investigation on the

26

target systems could be of key importance in order to obtain further insights into the influence of functionalizing species on the OER mechanism, as well as into the origin of selectivity against CER. Finally, future work will be addressed at the extension of the proposed synthetic approach to 3D electrodes supported on porous metallic foam substrates, as well as to OER-selective seawater electrolysis under neutral conditions, an additional open challenge for an ultimate real-world end-use.

Credit Authorship Contribution Statement

Lorenzo Bigiani: Conceptualization, Investigation, Formal analysis, Writing - original draft, Writing - review & editing

Davide Barreca: Conceptualization, Project administration, Funding acquisition, Supervision, Writing - review & editing

Alberto Gasparotto: Funding acquisition, Supervision, Validation, Writing - review & editing

Teresa Andreu: Investigation, Validation, Formal analysis, Writing - review & editing

Johan Verbeeck: Visualization, Funding acquisition, Writing - review & editing

Cinzia Sada: Investigation, Methodology, Formal analysis, Writing - review & editing

Evgeny Modin: Investigation, Methodology, Formal analysis

Oleg I. Lebedev: Investigation, Methodology, Formal analysis, Writing - review & editing

Juan Ramón Morante: Conceptualization, Supervision, Formal analysis, Writing - review & editing

Chiara Maccato: Conceptualization, Supervision, Funding acquisition, Formal analysis, Writing - review & editing

Declaration of competing interest

The authors declare that they have no competing financial interests, or personal relationships, that could have influenced the work reported in this paper.

Author contributions

L.B. carried out the plasma-assisted synthesis of the target materials and the electrochemical

27

experiments, in collaboration with T.A.; D.B, C.M, and J.R.M conceived the project and designed the experiments; A.G. and C.S. performed compositional analyses; C.M carried out and supervised FE-SEM and AFM analyses; J.V., E.M and O.I.L performed and interpreted TEM measurements.

Declaration of Competing Interest

The authors declare no conflict of interest.

Appendix A. Supplementary data

Supplementary material related to this article can be found, in the online version, at: https://doi.org/10.1016/j.apcatb.2xxx

References

[1]   J.G. Vos, T.A. Wezendonk, A.W. Jeremiasse, M.T.M. Koper, MnO_x/IrO_x as selective oxygen evolution electrocatalyst in acidic chloride solution, J. Am. Chem. Soc. 140 (2018) 10270-10281.

[2]   M.P. Browne, H. Nolan, B. Twamley, G.S. Duesberg, P.E. Colavita, M.E.G. Lyons, Thermally prepared $Mn_2O_3/RuO_2/Ru$ thin films as highly active catalysts for the oxygen evolution reaction in alkaline media, ChemElectroChem 3 (2016) 1847-1855.

[3]   Y.T. Meng, W.Q. Song, H. Huang, Z. Ren, S.Y. Chen, S.L. Suib, Structure-property relationship of bifunctional MnO_2 nanostructures: highly efficient, ultra-stable electrochemical water oxidation and oxygen reduction reaction catalysts identified in alkaline media, J. Am. Chem. Soc. 136 (2014) 11452-11464.

[4]   W. Tong, M. Forster, F. Dionigi, S. Dresp, R. Sadeghi Erami, P. Strasser, A.J. Cowan, P. Farràs, Electrolysis of low-grade and saline surface water, Nat. Energy 5 (2020) 367-377.

[5]   F. Song, L. Bai, A. Moysiadou, S. Lee, C. Hu, L. Liardet, X. Hu, Transition metal oxides as electrocatalysts for the oxygen evolution reaction in alkaline solutions: an application-Inspired renaissance, J. Am. Chem. Soc. 140 (2018) 7748-7759.

[6]   Y. Cheng, S.P. Jiang, Advances in electrocatalysts for oxygen evolution reaction of water electrolysis-from metal oxides to carbon nanotubes, Prog. Nat. Sci: Mater. Int. 25 (2015) 545-553.

[7]   R. Subbaraman, D. Tripkovic, K.-C. Chang, D. Strmcnik, A.P. Paulikas, P. Hirunsit, M. Chan, J. Greeley, V. Stamenkovic, N.M. Markovic, Trends in activity for the water electrolyser reactions on 3d M(Ni,Co,Fe,Mn) hydr(oxy)oxide catalysts, Nat. Mater. 11 (2012) 550-557.

[8]   H.A. Bandal, A.R. Jadhav, A.H. Tamboli, H. Kim, Bimetallic iron cobalt oxide self-supported on Ni-Foam: an efficient bifunctional electrocatalyst for oxygen and hydrogen evolution reaction, Electrochim. Acta 249 (2017) 253-262.

[9]   J. Juodkazytė, B. Šebeka, I. Savickaja, M. Petrulevičienė, S. Butkutė, V. Jasulaitienė, A. Selskis, R. Ramanauskas, Electrolytic splitting of saline water: durable nickel oxide anode for selective oxygen evolution, Int. J. Hydrogen Energy 44 (2019) 5929-5939.

[10]   M.A. Mansoor, M. Mazhar, V. McKee, Z. Arifin, Mn_2O_3-$4TiO_2$ semiconducting composite thin films for photo-electrochemical water splitting, Polyhedron 75 (2014)

29

135-140.

[11] L. Zeng, K. Zhou, L. Yang, G. Du, L. Liu, W. Zhou, General approach of in situ etching and doping to synthesize a nickel-doped M_xO_y (M = Co, Mn, Fe) nanosheets array on nickel foam as large-sized electrodes for overall water splitting, ACS Appl. Energy Mater. 1 (2018) 6279-6287.

[12] S. Dresp, F. Dionigi, M. Klingenhof, P. Strasser, Direct electrolytic splitting of seawater: opportunities and challenges, ACS Energy Lett. 4 (2019) 933-942.

[13] X. Lu, J. Pan, E. Lovell, T.H. Tan, Y.H. Ng, R. Amal, A sea-change: manganese doped nickel/nickel oxide electrocatalysts for hydrogen generation from seawater, Energy Environ. Sci. 11 (2018) 1898-1910.

[14] S. Dresp, F. Dionigi, S. Loos, J. Ferreira de Araujo, C. Spöri, M. Gliech, H. Dau, P. Strasser, Direct electrolytic splitting of seawater: activity, selectivity, degradation, and recovery studied from the molecular catalyst structure to the electrolyzer cell level, Adv. Energy Mater. 8 (2018) 1800338.

[15] D. Barreca, G. Carraro, A. Gasparotto, C. Maccato, M.E.A. Warwick, K. Kaunisto, C. Sada, S. Turner, Y. Gönüllü, T.-P. Ruoko, L. Borgese, E. Bontempi, G. Van Tendeloo, H. Lemmetyinen, S. Mathur, Fe_2O_3–TiO_2 nano-heterostructure photoanodes for highly efficient solar water oxidation, Adv. Mater. Interfaces 2 (2015) 1500313.

[16] P.-P. Liu, T.-T. Li, H.-L. Zhu, Y.-Q. Zheng, Manganese oxide with hollow rambutan-like morphology as highly efficient electrocatalyst for oxygen evolution reaction, J. Solid State Electrochem. 22 (2018) 2999-3007.

[17] Y. Zhao, B. Jin, A. Vasileff, Y. Jiao, S.-Z. Qiao, Interfacial nickel nitride/sulfide as a bifunctional electrode for highly efficient overall water/seawater electrolysis, J. Mater. Chem. A 7 (2019) 8117-8121.

[18] X. Song, T. Yang, H. Du, W. Dong, Z. Liang, New binary Mn and Cr mixed oxide electrocatalysts for the oxygen evolution reaction, J. Electroanal. Chem. 760 (2016) 59-63.

[19] B.A. Pinaud, Z.B. Chen, D.N. Abram, T.F. Jaramillo, Thin films of sodium birnessite-type MnO_2: optical properties, electronic band structure, and solar photoelectrochemistry, J. Phys. Chem. C 115 (2011) 11830-11838.

[20] R. Naeem, M.A. Ehsan, R. Yahya, M. Sohail, H. Khaledi, M. Mazhar, Fabrication of pristine Mn_2O_3 and Ag-Mn_2O_3 composite thin films by AACVD for photoelectrochemical water splitting, Dalton Trans. 45 (2016) 14928-14939.

[21] M.E.G. Lyons, M.P. Brandon, A comparative study of the oxygen evolution reaction on

oxidised nickel, cobalt and iron electrodes in base, J. Electroanal. Chem. 641 (2010) 119-130.

[22] W. Wang, L. Kuai, W. Cao, M. Huttula, S. Ollikkala, T. Ahopelto, A.-P. Honkanen, S. Huotari, M. Yu, B. Geng, Mass-production of mesoporous $MnCo_2O_4$ spinels with manganese(IV)- and cobalt(II)-rich surfaces for superior bifunctional oxygen electrocatalysis, Angew. Chem. Int. Ed. 56 (2017) 14977-14981.

[23] Z.S. Luo, E. Irtem, M. Ibanez, R. Nafria, S. Marti-Sanchez, A. Genc, M. de la Mata, Y. Liu, D. Cadavid, J. Llorca, J. Arbiol, T. Andreu, J.R. Morante, A. Cabot, $Mn_3O_4@CoMn_2O_4-Co_xO_y$ nanoparticles: partial cation exchange synthesis and electrocatalytic properties toward the oxygen reduction and evolution reactions, ACS Appl. Mater. Interfaces 8 (2016) 17435-17444.

[24] F. Mattelaer, T. Bosserez, J. Ronge, J.A. Martens, J. Dendooven, C. Detavernier, Manganese oxide films with controlled oxidation state for water splitting devices through a combination of atomic layer deposition and post-deposition annealing, RSC Adv. 6 (2016) 98337-98343.

[25] C.-H. Kuo, W. Li, L. Pahalagedara, A.M. El-Sawy, D. Kriz, N. Genz, C. Guild, T. Ressler, S.L. Suib, J. He, Understanding the role of gold nanoparticles in enhancing the catalytic activity of manganese oxides in water oxidation reactions, Angew. Chem. Int. Ed. 54 (2015) 2345-2350.

[26] Y. Gorlin, C.-J. Chung, J.D. Benck, D. Nordlund, L. Seitz, T.-C. Weng, D. Sokaras, B.M. Clemens, T.F. Jaramillo, Understanding interactions between manganese oxide and gold that lead to enhanced activity for electrocatalytic water oxidation, J. Am. Chem. Soc. 136 (2014) 4920-4926.

[27] O. Diaz-Morales, I. Ledezma-Yanez, M.T.M. Koper, F. Calle-Vallejo, Guidelines for the rational design of Ni-based double hydroxide electrocatalysts for the oxygen evolution reaction, ACS Catal. 5 (2015) 5380-5387.

[28] Y. Kuang, M.J. Kenney, Y. Meng, W.-H. Hung, Y. Liu, J.E. Huang, R. Prasanna, P. Li, Y. Li, L. Wang, M.-C. Lin, M.D. McGehee, X. Sun, H. Dai, Solar-driven, highly sustained splitting of seawater into hydrogen and oxygen fuels, PNAS 116 (2019) 6624.

[29] W.-H. Huang, C.-Y. Lin, Iron phosphate modified calcium iron oxide as an efficient and robust catalyst in electrocatalyzing oxygen evolution from seawater, Faraday Discuss. 215 (2019) 205-215.

[30] Y. Huang, L. Hu, R. Liu, Y. Hu, T. Xiong, W. Qiu, M.S. Balogun, A. Pan, Y. Tong, Nitrogen treatment generates tunable nanohybridization of Ni_5P_4 nanosheets with nickel

hydr(oxy)oxides for efficient hydrogen production in alkaline, seawater and acidic media, Appl. Catal., B: Environmental 251 (2019) 181-194.

[31]   F. Dionigi, T. Reier, Z. Pawolek, M. Gliech, P. Strasser, Design criteria, operating conditions, and nickel–iron hydroxide catalyst materials for selective seawater electrolysis, ChemSusChem 9 (2016) 962-972.

[32]   S. Fukuzumi, Y.-M. Lee, W. Nam, Fuel production from seawater and fuel cells using seawater, ChemSusChem 10 (2017) 4264-4276.

[33]   A. Ramírez, P. Hillebrand, D. Stellmach, M.M. May, P. Bogdanoff, S. Fiechter, Evaluation of MnO_x, Mn_2O_3, and Mn_3O_4 electrodeposited films for the oxygen evolution reaction of water, J. Phys. Chem. C 118 (2014) 14073-14081.

[34]   T. Okada, H. Abe, A. Murakami, T. Shimizu, K. Fujii, T. Wakabayashi, M. Nakayama, A bilayer structure composed of Mg|Co-MnO_2 deposited on a $Co(OH)_2$ film to realize selective oxygen evolution from chloride-containing water, Langmuir 36 (2020) 5227-5235.

[35]   R. Frydendal, E.A. Paoli, I. Chorkendorff, J. Rossmeisl, I.E.L. Stephens, Toward an active and stable catalyst for oxygen evolution in acidic media: Ti-stabilized MnO_2, Adv. Energy Mater. 5 (2015) 1500991.

[36]   D. Wintrich, D. Öhl, S. Barwe, A. Ganassin, S. Möller, T. Tarnev, A. Botz, A. Ruff, J. Clausmeyer, J. Masa, W. Schuhmann, Enhancing the selectivity between oxygen and chlorine towards chlorine during the anodic chlorine evolution reaction on a dimensionally stable anode, ChemElectroChem 6 (2019) 3108-3112.

[37]   F. Urbain, R. Du, P. Tang, V. Smirnov, T. Andreu, F. Finger, N. Jimenez Divins, J. Llorca, J. Arbiol, A. Cabot, J.R. Morante, Upscaling high activity oxygen evolution catalysts based on $CoFe_2O_4$ nanoparticles supported on nickel foam for power-to-gas electrochemical conversion with energy efficiencies above 80%, Appl. Catal., B: Environmental 259 (2019) 118055.

[38]   Y. Xiong, L. Xu, C. Jin, Q. Sun, Interface-engineered atomically thin Ni_3S_2/MnO_2 heterogeneous nanoarrays for efficient overall water splitting in alkaline media, Appl. Catal., B: Environmental 254 (2019) 329-338.

[39]   P. Gayen, S. Saha, V. Ramani, Selective seawater splitting using pyrochlore electrocatalyst, ACS Appl. Energy Mater. 3 (2020) 3978-3983.

[40]   T.P. Keane, D.G. Nocera, Selective production of oxygen from seawater by oxidic metallate catalysts, ACS Omega 4 (2019) 12860-12864.

[41]   Z. Morgan Chan, D.A. Kitchaev, J. Nelson Weker, C. Schnedermann, K. Lim, G. Ceder,

W. Tumas, M.F. Toney, D.G. Nocera, Electrochemical trapping of metastable Mn^{3+} ions for activation of MnO_2 oxygen evolution catalysts, PNAS 115 (2018) E5261-E5268.

[42]   R. Pokhrel, M.K. Goetz, S.E. Shaner, X. Wu, S.S. Stahl, The "best catalyst" for water oxidation depends on the oxidation method employed: a case study of manganese oxides, J. Am. Chem. Soc. 137 (2015) 8384-8387.

[43]   M. Jahan, S. Tominaka, J. Henzie, Phase pure α-Mn_2O_3 prisms and their bifunctional electrocatalytic activity in oxygen evolution and reduction reactions, Dalton Trans. 45 (2016) 18494-18501.

[44]   Q. Rui, L. Wang, Y. Zhang, C. Feng, B. Zhang, S. Fu, H. Guo, H. Hu, Y. Bi, Synergistic effects of P-doping and a MnO_2 cocatalyst on Fe_2O_3 nanorod photoanodes for efficient solar water splitting, J. Mater. Chem. A 6 (2018) 7021-7026.

[45]   J.E. Bennett, Electrodes for generation of hydrogen and oxygen from seawater, Int. J. Hydrogen Energy 5 (1980) 401-408.

[46]   K. Izumiya, E. Akiyama, H. Habazaki, N. Kumagai, A. Kawashima, K. Hashimoto, Effect of additional elements on electrocatalytic properties of thermally decomposed manganese oxide electrodes for oxygen evolution from seawater, Mater. Trans., JIM 38 (1997) 899-905.

[47]   K. Izumiya, E. Akiyama, H. Habazaki, N. Kumagai, A. Kawashima, K. Hashimoto, Mn-W oxide anodes prepared by thermal decomposition for oxygen evolution in seawater electrolysis, Mater. Trans., JIM 39 (1998) 308-313.

[48]   C. Liang, P. Zou, A. Nairan, Y. Zhang, J. Liu, K. Liu, S. Hu, F. Kang, H.J. Fan, C. Yang, Exceptional performance of hierarchical Ni–Fe oxyhydroxide@NiFe alloy nanowire array electrocatalysts for large current density water splitting, Energy Environ. Sci. 13 (2020) 86-95.

[49]   G. Carraro, C. Maccato, A. Gasparotto, K. Kaunisto, C. Sada, D. Barreca, Plasma-assisted fabrication of Fe_2O_3-Co_3O_4 nanomaterials as anodes for photoelectrochemical water splitting, Plasma Processes Polym. 13 (2016) 191-200.

[50]   P.-P. Liu, Y.-Q. Zheng, H.-L. Zhu, T.-T. Li, Mn_2O_3 hollow nanotube arrays on Ni foam as efficient supercapacitors and electrocatalysts for oxygen evolution reaction, ACS Appl. Nano Mater. 2 (2019) 744-749.

[51]   L. Bigiani, D. Zappa, C. Maccato, E. Comini, D. Barreca, A. Gasparotto, Quasi-1D MnO_2 nanocomposites as gas sensors for hazardous chemicals, Appl. Surf. Sci. 512 (2020) 145667.

[52]   D. Barreca, G. Carraro, E. Fois, A. Gasparotto, F. Gri, R. Seraglia, M. Wilken, A. Venzo,

A. Devi, G. Tabacchi, C. Maccato, Manganese(II) molecular sources for plasma-assisted CVD of Mn oxides and fluorides: from precursors to growth process, J. Phys. Chem. C 122 (2018) 1367-1375.

[53] D. Barreca, F. Gri, A. Gasparotto, G. Carraro, L. Bigiani, T. Altantzis, B. Žener, U. Lavrenčič Štangar, B. Alessi, D.B. Padmanaban, D. Mariotti, C. Maccato, Multi-functional MnO_2 nanomaterials for photo-activated applications by a plasma-assisted fabrication route, Nanoscale 11 (2019) 98-108.

[54] D. Barreca, A. Gasparotto, O.I. Lebedev, C. Maccato, A. Pozza, E. Tondello, S. Turner, G. Van Tendeloo, Controlled vapor-phase synthesis of cobalt oxide nanomaterials with tuned composition and spatial organization, CrystEngComm 12 (2010) 2185-2197.

[55] M. Pourbaix, *Atlas of electrochemical equilibria in aqueous solutions, 2nd English ed.* , Houston, Tex.: National Association of Corrosion Engineers, 1974.

[56] G.-F. Li, M. Divinagracia, M.F. Labata, J.D. Ocon, P.-Y. Abel Chuang, Electrolyte-dependent oxygen evolution reactions in alkaline media: electrical double layer and interfacial interactions, ACS Appl. Mater. Interfaces 11 (2019) 33748-33758.

[57] F. Lyu, Q. Wang, S.M. Choi, Y. Yin, Noble-metal-free electrocatalysts for oxygen evolution, Small 15 (2019) 1804201.

[58] W. Yang, Y. Peng, Y. Wang, Y. Wang, H. Liu, Z.a. Su, W. Yang, J. Chen, W. Si, J. Li, Controllable redox-induced in-situ growth of MnO_2 over Mn_2O_3 for toluene oxidation: active heterostructure interfaces, Appl. Catal., B: Environmental 278 (2020) 119279.

[59] F. Mou, L. Xu, H. Ma, J. Guan, D.-r. Chen, S. Wang, Facile preparation of magnetic γ-Fe_2O_3/TiO_2 Janus hollow bowls with efficient visible-light photocatalytic activities by asymmetric shrinkage, Nanoscale 4 (2012) 4650-4657.

[60] Pattern N° 024-0735, JCPDS (2000).

[61] Pattern N° 041-1442, JCPDS (2000).

[62] ICSD card N° 250541.

[63] ICSD card N° 36256.

[64] K. Fujimura, T. Matsui, K. Izumiya, N. Kumagai, E. Akiyama, H. Habazaki, A. Kawashima, K. Asami, K. Hashimoto, Oxygen evolution on manganese–molybdenum oxide anodes in seawater electrolysis, Mater. Sci. Eng. A 267 (1999) 254-259.

[65] A.A. El-Moneim, Mn–Mo–W-oxide anodes for oxygen evolution during seawater electrolysis for hydrogen production: effect of repeated anodic deposition, Int. J. Hydrogen Energy 36 (2011) 13398-13406.

[66] J.R. Galán-Mascarós, Water oxidation at electrodes modified with earth-abundant

transition-metal catalysts, ChemElectroChem 2 (2015) 37-50.

[67]   Z. Li, H. Li, Z. Wu, M. Wang, J. Luo, H. Torun, P. Hu, C. Yang, M. Grundmann, X. Liu, Y. Fu, Advances in designs and mechanisms of semiconducting metal oxide nanostructures for high-precision gas sensors operated at room temperature, Mater. Horiz. 6 (2019) 470-506.

[68]   K.S. Exner, H. Over, Beyond the rate-determining step in the oxygen evolution reaction over a single-crystalline $IrO_2(110)$ model electrode: kinetic scaling relations, ACS Catal. 9 (2019) 6755-6765.

[69]   Z. Sun, Y. Zhang, Y. Liu, J. Fu, S. Cheng, P. Cui, E. Xie, New insight on the mechanism of electrochemical cycling effects in MnO_2-based aqueous supercapacitor, J. Power Sources 436 (2019) 226795.

[70]   Q. Zhou, M. Zeng, X. Wu, Y. Zhang, G. Qin, Hierarchically porous core-shell microspheres assembled from Mn_2O_3/TiO_2 nanoparticles for enhanced lithium storage, J. Alloys Compounds 786 (2019) 368-376.

[71]   D.A. Tompsett, S.C. Parker, M.S. Islam, Rutile (β-)MnO_2 surfaces and vacancy formation for high electrochemical and catalytic performance, J. Am. Chem. Soc. 136 (2014) 1418-1426.

[72]   F. Ataherian, K.-T. Lee, N.-L. Wu, Long-term electrochemical behaviors of manganese oxide aqueous electrochemical capacitor under reducing potentials, Electrochim. Acta 55 (2010) 7429-7435.

[73]   F. Li, P. Wangyang, A. Zada, M. Humayun, B. Wang, Y. Qu, Synthesis of hierarchical Mn_2O_3 microspheres for photocatalytic hydrogen production, Mater. Res. Bull. 84 (2016) 99-104.

[74]   J. Wang, F.E. Osterloh, Limiting factors for photochemical charge separation in $BiVO_4/Co_3O_4$, a highly active photocatalyst for water oxidation in sunlight, J. Mater. Chem. A 2 (2014) 9405-9411.

[75]   B. Fuladpanjeh-Hojaghan, M.M. Elsutohy, V. Kabanov, B. Heyne, M. Trifkovic, E.P.L. Roberts, In-operando mapping of pH distribution in electrochemical processes, Angew. Chem. 131 (2019) 16971-16975.

[76]   L. Giordano, B. Han, M. Risch, W.T. Hong, R.R. Rao, K.A. Stoerzinger, Y. Shao-Horn, pH dependence of OER activity of oxides: current and future perspectives, Catal. Today 262 (2016) 2-10.